

We are IntechOpen, the world's leading publisher of Open Access books Built by scientists, for scientists

6,900

Open access books available

186,000

International authors and editors

200M

Downloads

Our authors are among the

154

Countries delivered to

TOP 1%

most cited scientists

12.2%

Contributors from top 500 universities



WEB OF SCIENCE™

Selection of our books indexed in the Book Citation Index
in Web of Science™ Core Collection (BKCI)

Interested in publishing with us?
Contact book.department@intechopen.com

Numbers displayed above are based on latest data collected.
For more information visit www.intechopen.com



Self-assembled Nanocomposite Oxide Films: Design, Fabrication, and Properties

Hao Yang^{1,2}, Qingquan Meng¹, Run Zhao¹, Jun Yang¹ and Weiwei Li¹

¹*School of Physical Science and Technology, Soochow University*

²*Materials Physics and Applications Division, Los Alamos National Laboratory*

¹China

²USA

1. Introduction

Nanocomposite metal oxides have been extensively investigated in bulk and thin film forms because of their wide range of applications in microelectronics, magneto electronics, and optoelectronics (Ramesh and Spaldin, 2007). Oxide films in nanocomposite form are particularly appealing as the interaction or coupling between the constituents can lead to enhanced or new functionalities (Zheng et al., 2006). Furthermore, the nanocomposite oxide films could lead to their applications as building blocks for the assembly of nanostructures or molecular monolayers (Cheng et al., 2006). A currently primary goal is to fabricate nanocomposite oxide films using a simple and low-cost process. Self-assembly has been the focus of much research in the last four decades. It has proved its ability to offer a rich variety of periodic nanoscale patterns in an easy way (Guiton and Davies, 2007). Recent efforts have striven to bring these two fields together. A major challenge is to control a self-assembled nanocomposite oxide film to create a desired nanostructure (Moshnyaga et al., 2003). In a film-on-substrate geometry, epitaxial composite films can be divided into two forms: horizontal and vertical. These two structures can be reviewed as the building blocks for a desired nanostructure and they are also specific architectures which show lots of potential applications (Yang et al., 2009). This chapter outlines the recent results about the material design, fabrication, and physical properties of these two nanostructures.

2. Material design

An important starting point for our studies was determining which systems have the potential to form clean, heteroepitaxial nanocomposite thin films with ordered nanostructures (MacManus-Driscoll et al., 2008). Since guidelines to the materials selection of nanocomposites have not been presented before, we developed our own as follows: (1) the chosen phases should both have the potential to grow epitaxially on a given substrate; (2) the growth kinetics of the individual phases should be similar so that the two phases can both grow with sufficient crystallinity at a chosen temperature; (3) the two phases of interest should be the most thermodynamically stable when the individual elements are combined; (4) cations with sufficiently different ionic radii are necessary to minimize intermixing of the

phases. It should be pointed out that these are only the necessary conditions for the material design and the sufficient conditions are underway.

3. Horizontal nanostructure

3.1 Overview

An oxide film with horizontal microstructure has also been viewed as a multilayer. Multilayers have been a basically interesting and technologically important research topic in recent years as they exhibit some remarkable and multifunctional properties that do not exist in either of their parents (Ueda et. al, 1998; Ohtomo et. al, 2002). A traditional way to fabricate multilayers is the alternative deposition of various types of thin layers. In the present work, we demonstrate a spontaneous, horizontal, multilayered, and heteroepitaxial oxide film in $(\text{YBa}_2\text{Cu}_3\text{O}_{7-x})_{0.5}:(\text{BaZrO}_3)_{0.5}$ nanocomposites (Yang et al., 2009). A high critical temperature of 88 K and a surprising field dependent of critical current along the *ab* plane were observed, given that the BaZrO_3 fraction in the films is 50 mol.%, which can be attributed to the self-assembled multilayer structure. The present study represents a new route to prepare multilayers of the oxide materials and holds great promise for other functional systems too.

3.2 Fabrication

Nanocomposite $(\text{YBCO})_{0.5}:(\text{BZO})_{0.5}$ (YBCO:BZO) films were grown on (001) oriented SrTiO_3 (STO) substrates by pulsed laser deposition (PLD) using a XeCl excimer laser ($\lambda=308$ nm). A single ceramic pellet with a molar ratio of YBCO/BZO = 1:1 was used as the target. A substrate temperature of 820°C and an oxygen pressure of 200 mTorr were maintained during the deposition. Following the deposition, the films were cooled down to room temperature in an oxygen pressure of 300 Torr without any further thermal treatment. The thickness of films, measured by the cross-sectional transmission electron microscopy (TEM), was 150 nm. The crystal structure was investigated by X-ray diffraction (XRD) using a Siemens D5000 four-circle diffractometer. The critical temperature (T_c) was evaluated by both alternating current (ac) susceptibility and transport measurement techniques. The critical current density (J_c) was obtained by the standard four-point method from a bridge using the 1 $\mu\text{V}/\text{cm}$ criterion, where the films were patterned using standard photolithography with a bridge width of ~ 250 μm . The angular and field dependent J_c measurements were conducted in a magnetic field (H) rotated in the plane perpendicular to the plane of the film but always normal to the current ($J \perp H$, maximum Lorentz force configuration). With the sample immersed in liquid nitrogen the measurement temperature was varied from 65 to 75.5 K.

3.3. Microstructures

Figure 1 shows a typical XRD θ - 2θ scan of the YBCO:BZO films. As can be seen from the figure, the YBCO and BZO phases are well defined and have comparable intensities, as broadly expected for the volume fractions and atomic weights of the compounds. The YBCO shows only (00 l) diffraction peaks and hence is preferentially oriented along the *c*-axis (perpendicular to the substrate surface). The *c* lattice constant of YBCO, calculated from the (005) peak, is 11.66(96) Å which is close to the bulk value of 11.6805 Å. The BZO shows (001) and (002) peaks, indicating the same *c*-axis orientation. It should be pointed out that besides

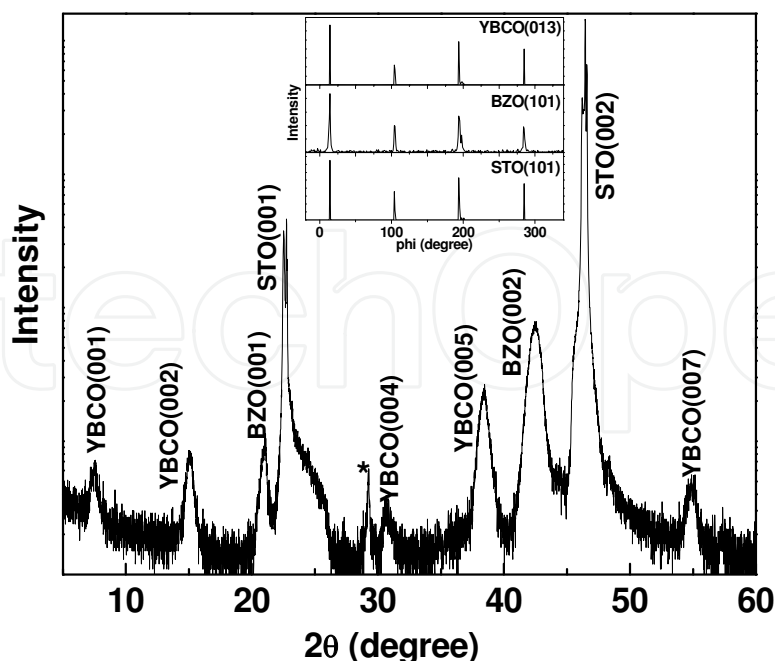


Fig. 1. Typical XRD θ - 2θ scan of YBCO:BZO films. A weak BZO (101) peak is denoted by a star. The inset shows phi-scans on STO (101), BZO (101), and YBCO (013) reflections.

the (00 l) peaks of YBCO and BZO, there is a weak peak at around $2\theta=29.4^\circ$ (shown with a star in Fig. 1) which can be attributed to BZO (101). By comparing the relative intensities of the Bragg peaks associated with the BZO (002) and BZO (101) peaks we estimate that $\sim 97\%$ of the BZO is c -axis oriented. The full-width at half-maximum (FWHM) of the rocking curves for YBCO (005) and BZO (002) are 1.24° and 0.86° , respectively. These values are higher than those for typical pure YBCO and BZO films and the large lattice mismatch between YBCO and BZO is likely responsible for this. The in-plane orientation of the YBCO:BZO films with respect to the major axis of the STO substrate is revealed by phi-scans on the YBCO (013), BZO (101), and STO (101) reflections (shown in the inset of Fig. 1). The orientation relationship is determined to be $(001)_{\text{YBCO}} \parallel (001)_{\text{BZO}} \parallel (001)_{\text{STO}}$ and $[010]_{\text{YBCO}} \parallel [010]_{\text{BZO}} \parallel [010]_{\text{STO}}$, which is in accordance with the pure YBCO and BZO thin films grown on STO substrates.

In order to reveal the detailed microstructure of the YBCO:BZO films, low magnification and high resolution cross-sectional TEM were performed. As can be seen from the low magnification bright-field TEM image (Fig. 2), a multilayer structure is formed throughout the film, i.e., spontaneously ordered alternating layers of YBCO and BZO. The YBCO and BZO layers show thicknesses of 6-10nm and 7-11 nm, respectively. All the layers are continuous in-plane (lateral dimension) up to a micro-meter scale. This is the first time a self-assembled, ordered horizontal nanocomposite film has been observed, although we have observed a self-assembled vertical analogue before in another perovskite system (MacManus-Driscoll et al., 2008; Yang et al., 2009). For YBCO films with BZO, the microstructures previously observed are either random BZO nanoparticles or self-assembled columnar BZO nanorods (MacManus-Driscoll et al., 2004; Kang et al., 2006; Maiorov et al., 2009). The completely different microstructure in the present study originates from an interplay between composition, strain, and growth kinetics (MacManus-Driscoll et al., 2008).

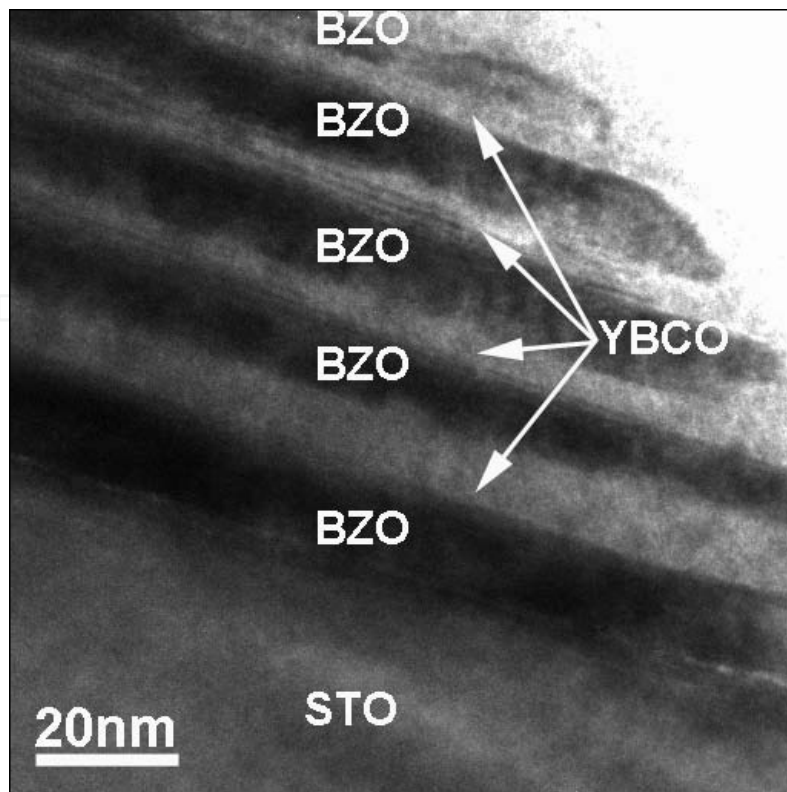


Fig. 2. A low magnification bright field TEM image of a nanocomposite YBCO:BZO film on STO substrate.

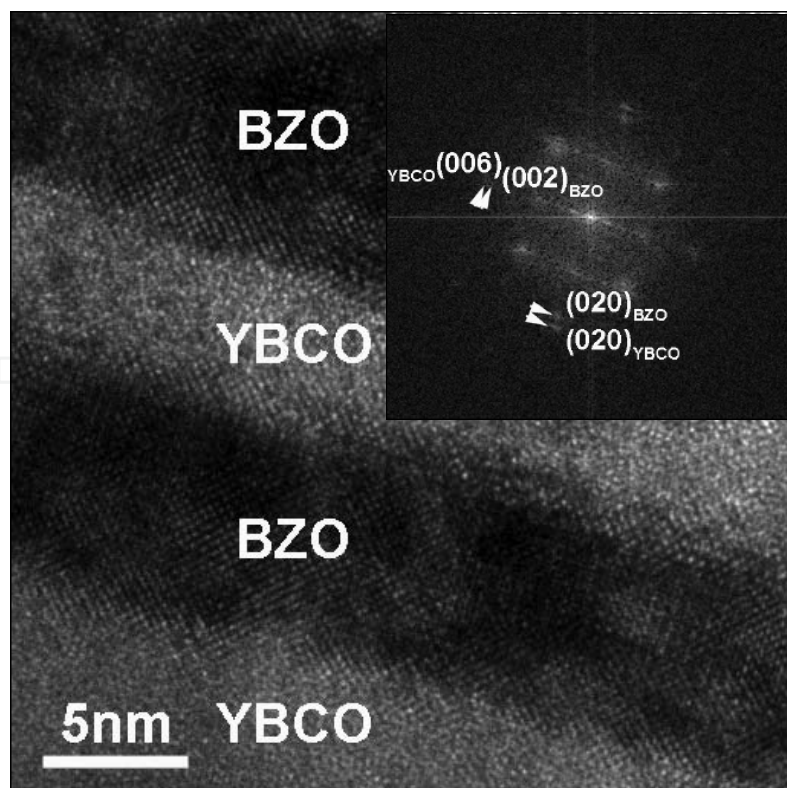


Fig. 3. High resolution TEM image with corresponding fast Fourier filtered (FFT) image at the YBCO/BZO interface.

A high resolution TEM (HRTEM) image (Fig. 3) reveals excellent heteroepitaxial growth between the YBCO and BZO layers. The corresponding fast Fourier transformed image from the interface of YBCO and BZO is shown in the inset of Fig. 3. The orientation relations of the YBCO/BZO multilayers are determined to be $(001)_{\text{YBCO}} \parallel (001)_{\text{BZO}}$ and $[010]_{\text{YBCO}} \parallel [010]_{\text{BZO}}$, which is consistent with the results from XRD measurements. It is well known that there is a close relationship between the superconductivity and the microstructure in YBCO films (Foltyn et al., 2007). This micron scaled-continuous self-assembled nanolayer structure are believed to contribute to the unique physical properties of YBCO:BZO films.

3.4 Physical properties

It is known that power applications of superconductors require an effective immobilization of vortices, or in other words a high pinning force (Foltyn et al., 2007). The pinning force arises from the presence of localized defects or crystalline imperfections. It has been experimentally shown that nanoscale defects within YBCO materials can pin the magnetic flux lines which translates to a high critical current density (J_c). Recent efforts have focused on non-superconducting additions to YBCO films to enhance the current carrying capability in applied magnetic fields. For example, Y_2O_3 , CeO_2 , YBa_2CuO_5 , and BZO, because of their good compatibility with YBCO, have been effectively used to increase J_c in YBCO films (Barnes et al., 2004; Haugan et al., 2004). In general, the increase of the BZO content (or the density of pinning sites) initially increases the macroscopic J_c , but beyond some optimum density the performance deteriorates. For this purpose, the critical temperature (T_c) and the J_c of YBCO film with different levels of BZO inclusion have been widely investigated. It is a common view that the T_c decreases linearly with increasing BZO concentration (Kang et al., 2007; Peurla et al. 2006). Currently, the reported maximum inclusion of BZO in YBCO films is 8 vol.% (~18 mol.%) where a T_c of 82.8 K was observed. For this concentration, BZO self-assembles in vertical columns along the c -axis (Kang et al., 2007). A question that arises is,

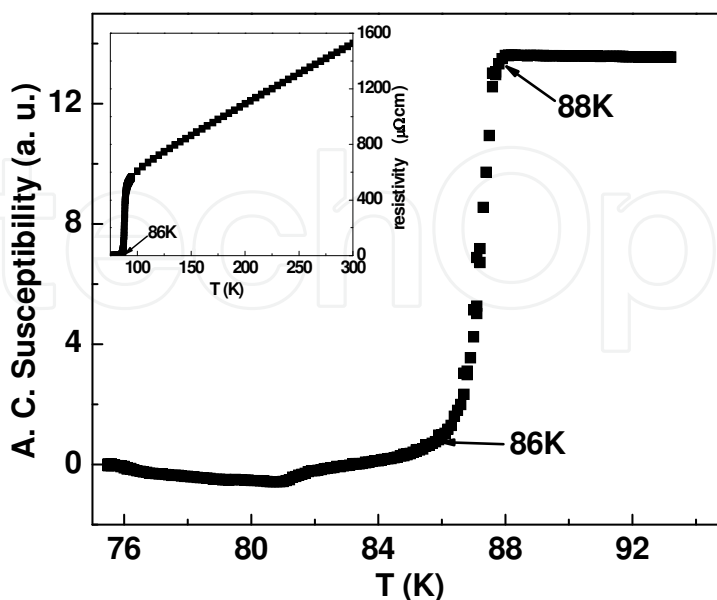


Fig. 4. Ac susceptibility of a nanocomposite YBCO:BZO film. The inset shows the resistivity versus temperature characteristic of the same film.

what will happen to the superconductivity of a YBCO film when the BZO inclusion is more than 18 mol.%? It is important to investigate the superconductivity of YBCO:BZO films and the relationship between the physical properties and the unique horizontal nanostructure.

The temperature dependence of ac susceptibility of YBCO:BZO film is shown in Fig. 4. A clear superconducting transition was observed and the on-set T_c was determined to be 88 K which is much higher than the reported value of YBCO films with only 18 mol.% BZO (Kang et al., 2007; Peurla et al., 2006). To confirm the high T_c , the temperature dependence of resistivity measurement was conducted and shown as inset of Fig. 4. A typical linear relationship was found above the transition temperature. The zero resistance temperature of 86 K from the transport measurement agrees well with the result obtained from the ac susceptibility measurement. The resistivity values of the YBCO:BZO film, 600 and 1500 $\mu\Omega\cdot\text{cm}$ at 100 and 300 K respectively, are one order of magnitude higher than those of a typical pure YBCO film. The layered structure and the highly resistive nature of the BZO lead to the high resistivity of the nanocomposite films. Considering the multilayer structure in the YBCO:BZO films, a T_c of 88 K is not completely unexpected. Huhtinen *et al.* represented a systematic investigation of superconductivity of YBCO/BZO multilayers fabricated from two different targets by PLD (Huhtinen et al., 2009). T_c s from 88 K to 89.3 K have been observed which dependent on the thickness of BZO layer relative to the YBCO layer and agree well with our results. It should be pointed out that multilayers have been found to increase the density of misfit dislocations at the layer interfaces which compensate the mismatch between YBCO and BZO lattices in the current study (Jia et al., 2002; Pan et al., 2006). This is the main reason that the c lattice constant of YBCO phase is close to the bulk value which also contributes to the high T_c value (Huhtinen et al., 2009).

To investigate the flux pinning properties of the YBCO:BZO films, the magnetic field (H) dependence of J_c was measured at 65 K and shown in Fig. 5. J_c is normalized to self-field value ($J_c(sf)=0.15 \text{ MA/cm}^2$) to facilitate the comparison. Firstly, a most striking feature is observed for the case of $H//ab$, which has an extremely slow J_c field decay. The α value in

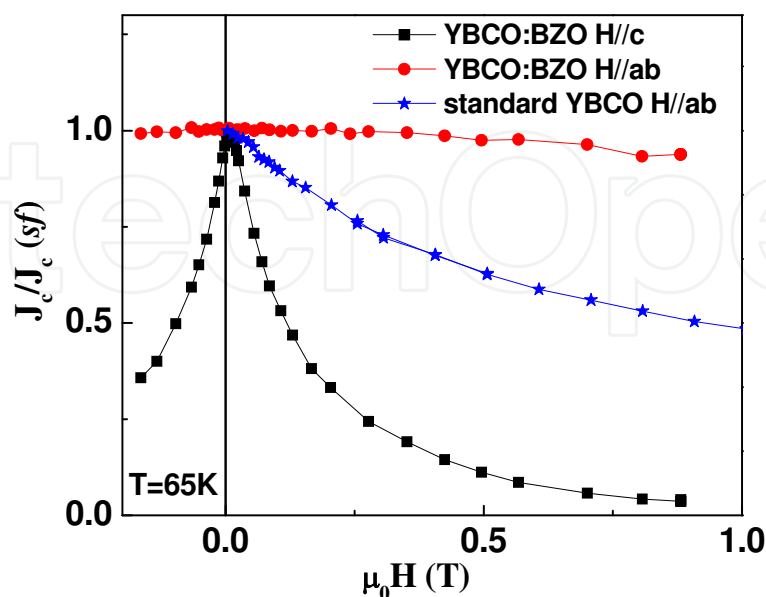


Fig. 5. Magnetic field dependence of J_c of a nanocomposite YBCO:BZO film at 65 K. For comparison, a curve for standard pure YBCO films is also included.

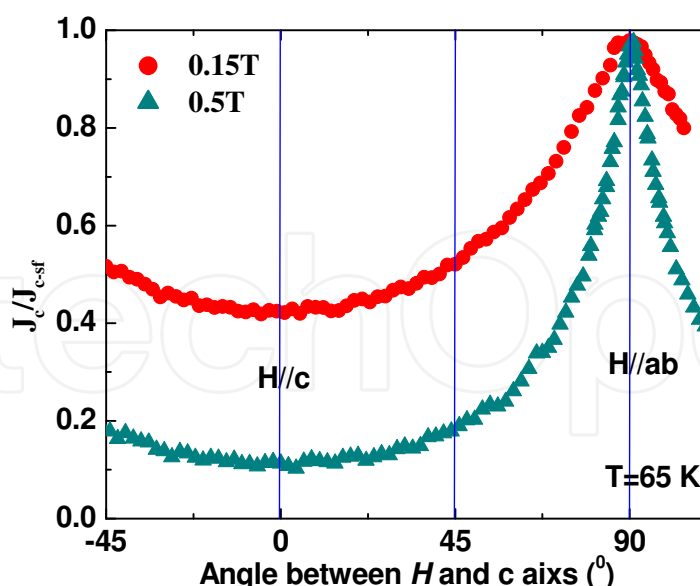


Fig. 6. The angular dependence of J_c of a nanocomposite YBCO:BZO film at 65 K and with applied magnetic field of 0.15 and 0.5 T.

the relation of $J_c \sim H^{-\alpha}$ was calculated to be 0.06, which is much lower than the typical value of pure YBCO film (~ 0.51) and indicates a weaker field dependence of J_c . Secondly, for $H//c$ $J_c(H)$ drops much faster than standard pure YBCO with a α value of 1.48. For the lower concentration doping of BZO in YBCO films, BZO have been reported to self-assemble in vertical columns along the c -axis. And α values from 0.31 to 0.61 have been observed (Kang et al., 2006). By comparing these values with those in the current study, we can see the much lower density of defect along c axis and much higher density of defect along ab plane in the nanocomposite YBCO:BZO film, which is confirmed by the multilayer structure. It should be pointed out that the $J_c(sf)$ value here is comparable to the reported results of YBCO/BZO multilayers fabricated by two different targets using PLD and could be related to the high resistivity observed.¹⁴ The angular dependence of J_c was also measured and shown as Fig. 6. An enhanced peak for $H//ab$ was observed compared to the typical pure YBCO films and no peak was found for $H//c$, which are consistent with the multilayer structure and the reported results (Cai et al., 2004).

To summarize, nanocomposite $(\text{YBCO})_{0.5}:(\text{BZO})_{0.5}$ thin films were fabricated by PLD. Both YBCO and BZO phases exhibited spontaneous, horizontal, multilayered, and heteroepitaxial phase assemblage. This unique microstructure led to a T_c of 88 K and a surprising field dependence of J_c along the ab plane. The present study represents a new route to prepare horizontal structures of the oxide films and holds great promise for other functional materials too.

4. Vertical nanostructure

4.1 Overview

Nanocomposite films with a vertical architecture such as the nanopillar geometry offer numerous advantages over the conventional horizontal multilayers, such as a larger interfacial area and intrinsic heteroepitaxy in three dimensions (Zheng et al., 2004; Ramesh et al., 2007). Moshnyaga et al. firstly showed vertical nanopillar films with a composition of

$(\text{La}_{0.7}\text{Ca}_{0.3}\text{MnO}_3)_{1-x}:(\text{MgO})_x$ (Moshnyaga et al., 2003). The structural and magnetotransport properties of the $\text{La}_{0.7}\text{Ca}_{0.3}\text{MnO}_3$ nanoclusters were tuned through the tensile stress originating from the MgO second phase. Zheng et al. reported vertical nanostructures consisting of magnetic spinel CoFe_2O_4 pillars epitaxially embedded into a ferroelectric BaTiO_3 matrix (Zheng et al., 2004). This nanocomposite exhibited strong coupling of the ferroelectric and magnetic order parameters through the three-dimensional heteroepitaxy of the two lattices.

Vertical nanocomposite architectures are not only interesting for achieving multifunctionality, but there is also the potential for enhancing a single functionality through manipulation of the strain of one of the phases by another. Horizontal (lateral) strain within layered heterostructures has been widely studied and indeed is fundamental to many semiconductor device technologies. Recent work has shown that strain control of very thin oxide films can achieve dramatically enhanced functional properties: strain fields perturb ferroelectricity (Nagarajan et al., 2005), and huge changes in the ferroelectric Curie temperature T_c , remanent polarization and structural phase transition temperature have been demonstrated in SrTiO_3 and BaTiO_3 through use of substrate-controlled, coherent in-plane biaxial strain (Haeni et al., 2004; Choi et al., 2004). While such lateral strain control experiments are elegant, the thickness over which substantial strains can be maintained is seriously limited, meaning that use of lateral strain control for any potential applications is restricted. Coherently strained films in which the film and substrate in-plane lattice parameters are identical can be maintained only up to a critical thickness (t_c), which is on the order of a few nanometres, depending on the amount of the misfit. Above t_c , the strain energy becomes so large that it is then energetically favorable to nucleate misfit dislocations (Matthews et al., 1974).

Given this, and that self-assembled vertical nanocomposite systems have enormous potential to control strain vertically in much thicker films with correspondingly large volume, it is surprising that vertical strain control has not been explored previously. In this chapter, $(\text{BiFeO}_3)_{0.5}:(\text{Sm}_2\text{O}_3)_{0.5}$ nanocomposite thin films have been fabricated by PLD, where both BiFeO_3 (BFO) and Sm_2O_3 (SmO) phases are spontaneously self-assembled into a vertically ordered nano-columnar structure. The microstructures and vertical interface effects on physical properties are demonstrated.

4.2 Fabrication

Epitaxial nanocomposite $(\text{BiFeO}_3)_{0.5}:(\text{Sm}_2\text{O}_3)_{0.5}$ (BFO:SmO) films were grown on (001) oriented STO and Nb-doped SrTiO_3 (Nb-STO) substrates by PLD using a XeCl excimer laser ($\lambda=308$ nm). A single ceramic pellet with a molar ratio of $0.5(\text{BiFeO}_3)-0.5(\text{Sm}_2\text{O}_3)$ was used as the target. BFO:SmO were grown at 670°C with a XeCl excimer laser operated at 5 Hz laser repetition rate, and at 100 mtorr oxygen pressure. The thickness of films, measured by cross-sectional TEM, was 150 nm. For comparison, pure BFO and SmO thin films with the same thickness were also deposited on (001) oriented STO and Nb-STO substrates using the same processing parameters. It should be noted that the single-crystal conductive Nb-STO substrate not only provides a good template for epitaxial growth of BFO, SmO, and BFO:SmO films, but also functions as a bottom electrode for the electrical measurements. The crystal structures of thin films were investigated by high-resolution XRD (HRXRD) and TEM. Nuclear resonance backscattering spectrometry with a He^+ beam energy of 3.045 MeV was used to measure oxygen concentration in the pure BFO film. Compared with traditional Rutherford backscattering spectrometry, the strong and narrow resonance

provides a better sensitivity and depth resolution for oxygen detection. In our measurement, the beam energy was chosen in a way that resonant scattering occurs in the film not in the substrate. For electrical property measurements, vertical sandwich capacitors with a configuration of Pt/BFO:SmO/Nb-STO (or Pt/BFO/Nb-STO, Pt/SmO/Nb-STO) were fabricated, where the Pt top electrodes with an area of $1 \times 10^{-4} \text{ cm}^2$, defined by a lift-off lithography process, were deposited by sputtering. The frequency dependent capacitance ($C-f$) and dielectric loss ($\tan \delta-f$) were measured using a HP4194A impedance analyzer. The current-voltage ($I-V$) characteristics of the capacitors were measured using a Keithley 487 picoampere meter with a delay time of 5 seconds.

4.3 Microstructures

In order to reveal the microstructure of self-assembled BFO:SmO nanocomposites, plan-view and cross-sectional transmission electron microscopy was performed. As can be seen from the plan-view TEM image (Fig. 7a), a checker-board structure is formed. In other words, an ordered alternative growth of BFO and SmO domains (marked as B and S, respectively) is self-assembled. Each of the domains has a lateral dimension of $\sim 15 \text{ nm}$. A low magnification bright-field cross-sectional TEM image (Fig. 7b) also shows that the BFO and SmO domains have grown alternately and vertically aligned with an average column size of 15 nm . A high resolution TEM (HRTEM) image (Fig. 7c) reveals excellent heteroepitaxial growth of the BFO and SmO nanocolumns on the STO substrate. It is interesting to note that there is a lattice matching relation along the vertical boundaries between the BFO and SmO. The matching spacing is about 1.3 nm . The corresponding fast Fourier transformed images from the areas of the BFO, SmO and STO are shown as an insert of Fig. 7c. The orientation relations of the BFO:SmO nanocomposite and the substrate are determined to be $(002)_{\text{BFO}} // (004)_{\text{SmO}} // (002)_{\text{STO}}$ and $[200]_{\text{BFO}} // [440]_{\text{SmO}} // [200]_{\text{STO}}$, which is in accordance with the pure BFO and SmO thin films grown on STO substrates. The BFO:SmO nanocomposite thin film provides the opportunity to investigate the vertical interface effect on the physical properties of the individual BFO and SmO phases by comparison to the pure-phase films.

4.4 Physical properties

For epitaxial metal oxide films, interfaces always play a critical role in controlling the structural and electrical properties. Both experimental and theoretical works have demonstrated the impact of lateral interface on the physical properties of either single-phase thin films or superlattices (Junquera et al., 2003; Ohtomo et al., 2004; Choi et al., 2004; Reyren, et al., 2007). For instance, Reyren *et al.* reported superconductivity in the electron gas formed at the interface between LaAlO_3 and SrTiO_3 (Reyren et al., 2007). There have also been reports on the lateral interface effect on the physical properties of ferroelectric thin films, such as size effects, critical thickness, and strain and coupling enhanced ferroelectricity (Lee et al., 2005; Jia et al., 2007). Compared with the lateral interface, the effect of vertical interface on the physical properties of metal oxide films is profound. However, there are only a few reports because of the lack of vertical nanocomposites with ordered structures on a large scale (Ramesh et al., 2007). Here we demonstrate the vertical interface effect on lattice parameters, dielectric properties, and leakage current of BFO:SmO nanocomposite films. To illustrate the improved functionalities of our nanocomposites, we compare to the physical properties of pure BFO and SmO thin films.

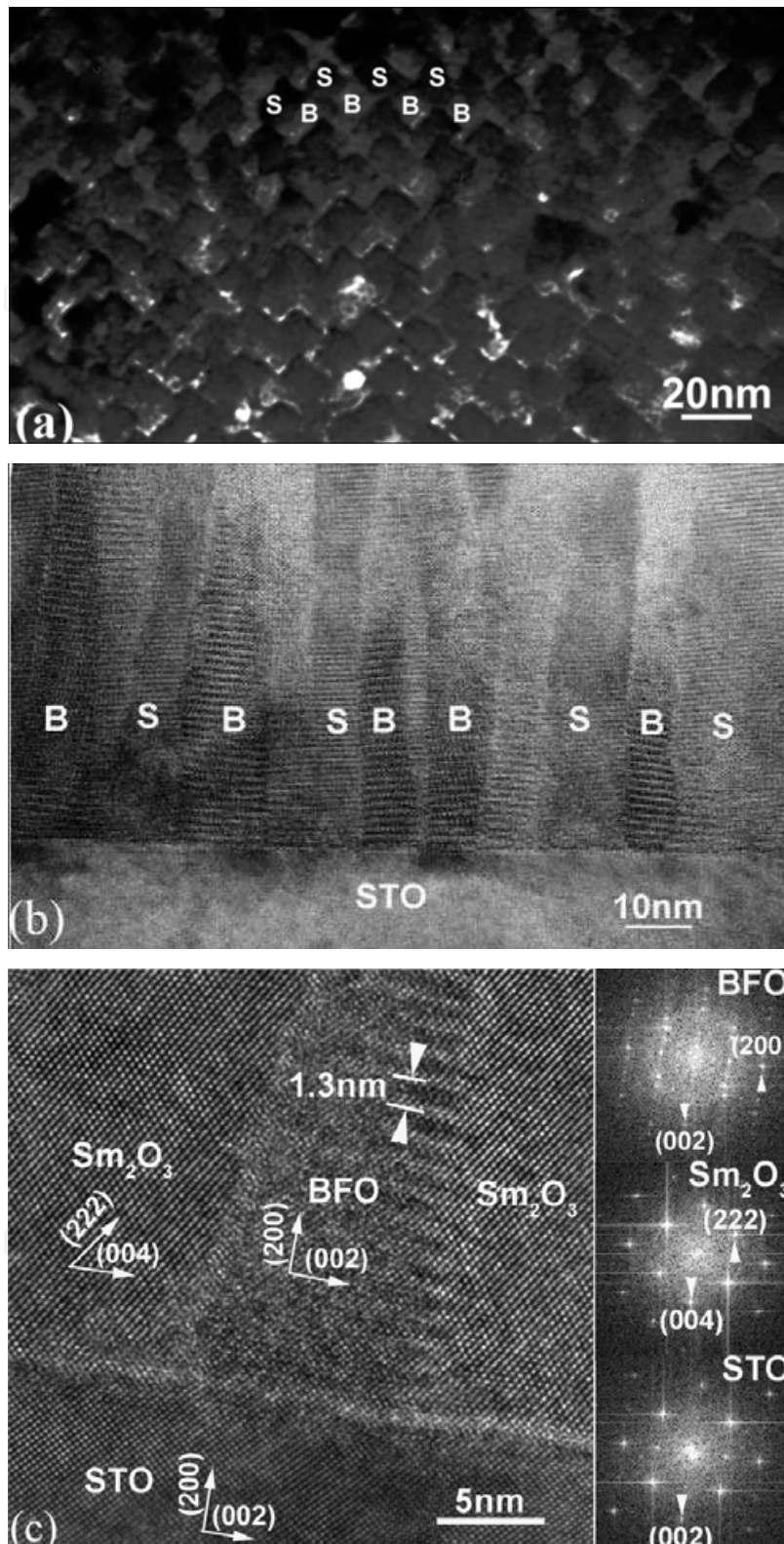


Fig. 7. TEM images of the BFO:SmO nanocomposite film on an STO substrate: (a) Plan-view showing an ordered checker-board structure (B represents BFO, S represents SmO); (b) low magnification cross-sectional view showing the alternating columns of BFO and SmO; (c) high resolution cross-sectional view with corresponding fast Fourier filtered (FFT) images from BFO, SmO and STO areas.

	BFO:SmO nanocomposite film		pure BFO thin film	pure SmO thin film	Bulk BFO	Bulk SmO
	BFO	SmO				
out-of-plane lattice constant (Å)	3.905	11.088	3.981	10.886	3.962	10.920

Table 1. Out-of-plane lattice constants of individual BFO and SmO phases in the BFO:SmO nanocomposite film, and pure BFO and SmO thin films on STO or Nb-STO substrates. The thicknesses of all the films are 150 nm. Bulk values are also shown.

Table 1 shows the out-of-plane lattice constants of individual BFO and SmO phases in the BFO:SmO nanocomposite. In comparison, lattice parameters of pure BFO and SmO thin films and bulk values of BFO and SmO are also included in the table. The out-of-plane lattice constant of the BFO phase in the nanocomposite is 3.905 Å, compared with a value of 3.981 Å and 3.962 Å for the pure BFO film and the bulk BFO respectively. It should be noted that the BFO phase in the nanocomposite is under compressive strain (-1.46%) in contrast with a tensile strain (+0.47%) for the pure BFO film. On the other hand, the vertical strain state of SmO phase in the nanocomposite is switched from compression (-0.31%) to tension (+1.54%), opposite to the strain switching in the BFO phase. It is apparent that the dominant strain mechanism for the BFO and SmO phases arises from the vertical interface, rather than from the lateral interface. As the absolute values of the vertical strain in the nanocomposite are 3-5 times of those in the pure films, the vertical interface is more efficient to control the out-of-plane lattice constant than the lateral interface.

To understand the vertical interface effect on the electrical properties of the nanocomposite, we measured the dielectric properties of BFO:SmO, BFO, and SmO thin films. As can be seen from the TEM images, the BFO and SmO columns of the nanocomposite are connected in parallel if one considers a vertical capacitor structure of Pt/BFO:SmO/Nb-STO. Sherman *et al.* have studied the dielectric properties of the columnar composite by using an equivalent electrical circuit consisting of two capacitors connected in parallel (Sherman *et al.*, 2006; Yamada *et al.*, 2006). In the case of our (BFO)_{0.5}:(SmO)_{0.5} nanocomposite films, if we assume the equal surface area of two different phases (see the TEM image), the dielectric constant and dielectric loss can be expressed as:

$$\epsilon_{BFO:SmO} = \frac{1}{2}(\epsilon_{BFO} + \epsilon_{SmO}) \quad (1)$$

$$\tan \delta_{BFO:SmO} = \frac{\epsilon_{BFO} \tan \delta_{BFO} + \epsilon_{SmO} \tan \delta_{SmO}}{\epsilon_{BFO} + \epsilon_{SmO}}, \quad (2)$$

where, the $\epsilon_{BFO:SmO}$, ϵ_{BFO} , and ϵ_{SmO} are the dielectric constants of the BFO:SmO nanocomposite film, the pure BFO film, and the pure SmO film. The $\tan \delta_{BFO:SmO}$, $\tan \delta_{BFO}$, and $\tan \delta_{SmO}$ are the dielectric losses of the BFO:SmO nanocomposite film, the pure BFO film, and the pure SmO film. Because there is no observable intermixing of two individual phases from the HRTEM image, we ignore any reactive products between the BFO and the SmO in nanocomposite film. It is noted that there is the possibility of some Sm³⁺ substitution for Bi³⁺ in the BFO nanocolumns, but this isovalent substitution should not alter the dielectric or leakage properties of the film since no charge compensating defects would be

required to form. Fig. 8a shows the measured dielectric constants of BFO:SmO, BFO, and SmO thin films as a function of frequency. The calculated dielectric constant of the nanocomposite from Eq. (1) is 92. The difference between the experimental and calculated dielectric constants of BFO:SmO nanocomposite film is about 4%.

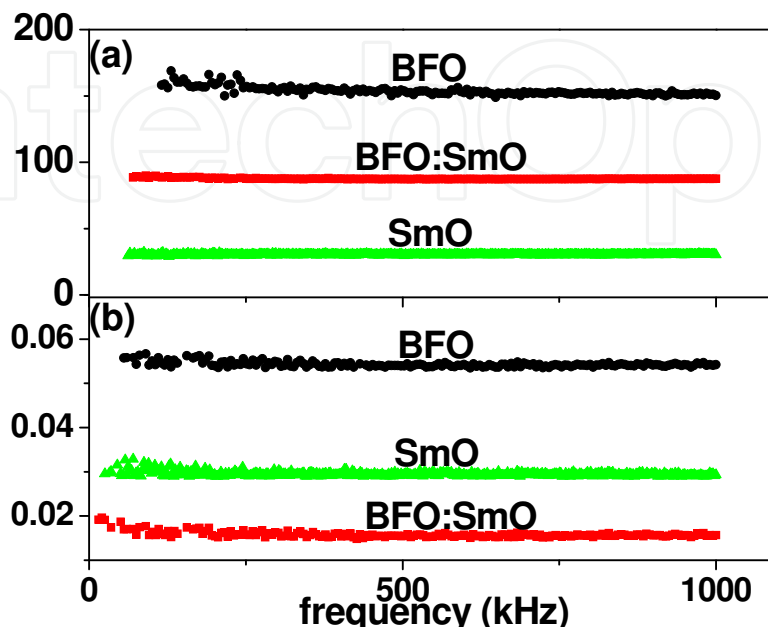


Fig. 8. Dielectric constants (a) and dielectric losses (b) of BFO:SmO, BFO, and SmO thin films as a function of frequency.

Thus, the dielectric constant of such a BFO:SmO nanocomposite can be well described by an equivalent parallel circuit model. In other words, considering that the dielectric constant of the nanocomposite should be controlled by the higher dielectric constant phase, the strong vertical strain of BFO phase shows little influence on the dielectric constant of the nanocomposite. This is possible considering that BFO has a high Curie temperature (~ 1103 K) (Michel et al., 1969). For ferroelectric materials at a temperature (300 K in this case) that is far away from the Curie temperature, the strain shows little influence on the dielectric properties directly.

Fig. 8b shows the dielectric losses of BFO:SmO, BFO, and SmO thin films as a function of frequency. The calculated dielectric loss of BFO:SmO nanocomposite from Eq. (2) is 0.050, which is much larger than the experimental value of 0.015. It is interesting to consider the source of the large reduction in the dielectric loss of the BFO:SmO nanocomposite. As can be seen from Eq. (2), the reduction of the dielectric loss must originate from the BFO phase, since the dielectric properties of the BFO phase should control the overall dielectric properties of the nanocomposite. It has been widely reported that there is a close relationship between leakage current and dielectric loss in ferroelectric materials. Ferroelectric materials with lower leakage current typically exhibited smaller dielectric loss (Joshi, et al., 2000). For example, Wang *et al.* reported that reduction of oxygen vacancies in doped BFO films reduced the leakage current and then the dielectric loss (Wang et al., 2006). Figure 9 shows the leakage current density *vs.* electric field (*J-E*) characteristics of BFO:SmO, BFO, and SmO thin films. Because the leakage current density of the SmO thin film at low electric fields reaches the limit of our measurement, we only show the leakage current

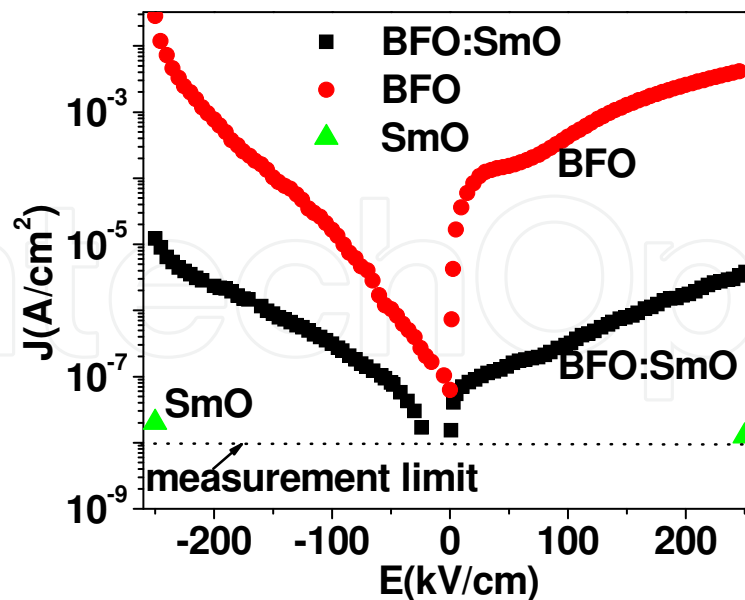


Fig. 9. Leakage current density *vs.* electric field (*J-E*) characteristics of BFO:SmO, BFO, and SmO thin films. The dotted line shows the measurement limit.

density at an electric field of ± 250 kV/cm. As illustrated in Fig. 9, the resistivity (ρ) of different films at a given electric field follows the relationship: $\rho_{\text{SmO}} \gg \rho_{\text{BFO:SmO}} \gg \rho_{\text{BFO}}$. If we consider BFO and SmO columns in the BFO:SmO nanocomposite as resistors connected in parallel with a device configuration of Pt/BFO:SmO/Nb-STO, the leakage current will be controlled by the BFO because of the much higher resistance of SmO. In other words, the leakage current of the BFO phase within the nanocomposite will be roughly the same as the total leakage current of the entire BFO:SmO nanocomposite film. This implies that the leakage current density of the BFO phase in the nanocomposite film is much lower than that of a pure BFO film. This may explain the much lower experimentally observed dielectric loss of the nanocomposite film relative to the loss calculated from Eq. (2).

It is important to investigate the origin of the reduction of the leakage current density of the BFO phase in the nanocomposite film. It has been widely reported that oxygen vacancies (V_{O}), rather than Fe^{2+} ions, are the main cause of high leakage current densities in BFO thin films. Efforts have been made to reduce the V_{O} by introducing post-annealing in an oxygen atmosphere, doping with higher valence ions, and oxygen ion implanting (Wang, et al., 2006). To investigate the oxygen vacancies effect on the leakage current density in the present study, some pure BFO films and BFO:SmO nanocomposites were subjected to an in situ annealing in oxygen (~ 500 Torr) at a temperature of 390°C for 60 mins. Nuclear resonance backscattering spectrometry (NRBS) was used to measure the oxygen concentration in the as-deposited and annealed BFO films (as shown in Fig. 10). In principle, NRBS is identical to the well known Rutherford backscattering spectrometry, with an exception that higher projectile beam energy is used in NRBS. Higher energy allows the interaction between the projectile and the target nucleus to overcome the Coulomb repulsive force barrier due to a very close encounter between incident particle and the target nucleus. As a result, the scattering cross section becomes non-Rutherford and often exhibits a narrow

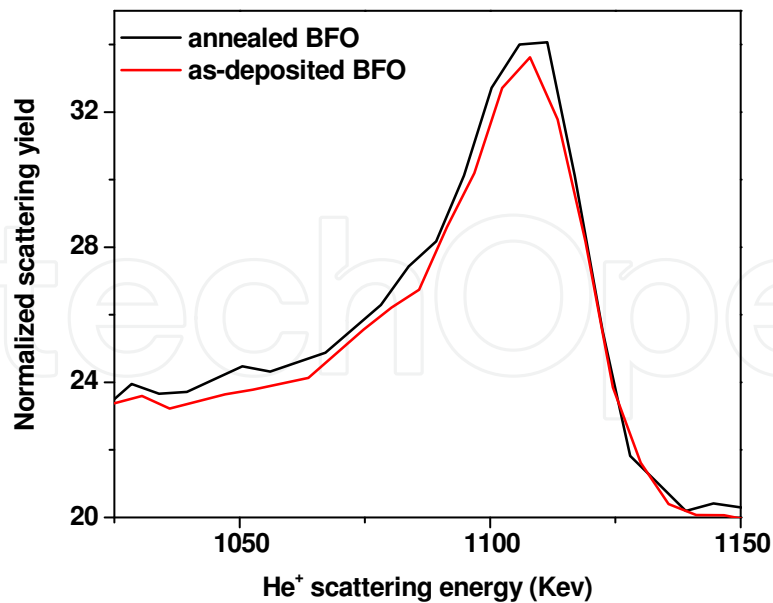


Fig. 10. Oxygen resonance peaks of as-deposited and annealed BFO films.

and strong resonance peaks that sometimes can be orders of magnitude stronger than the Rutherford value. Multiple light elements such as B, C, N, and O can be measured with NRBS simultaneously. In our measurement, the beam energy was chosen in a way that resonant scattering occurs in the film (not in the substrate). Compared with traditional Rutherford backscattering spectrometry using 2 MeV He⁺ beam, the strong and narrow resonance at 3.045 MeV provides a better sensitivity (~10 times better) for oxygen detection. Oxygen concentration was determined by fitting oxygen peak in the measured spectrum using SIMNRA, popularly used data reduction software in ion beam analysis. Resonance scattering cross sections in the SIMNRA database was cross-checked using a known oxygen standard such as a bare STO substrate. The oxygen concentration is determined to be 5.14×10^{17} and 5.44×10^{17} at./cm² for as-deposited and annealed BFO films, respectively. The ideal oxygen concentration for stoichiometric BFO film is estimated to be 5.79×10^{17} at./cm². The NRBS results clearly show that there are V_{Os} in BFO films: 11.2% deficient in the as-deposited film and 6.0% deficient in post-annealed film compared to the ideal case. At the same time, the V_{Os} can be effectively reduced by the post-annealing which is consistent with reported results (Wang et al., 2006). Furthermore, the leakage current densities of as-deposited and annealed BFO and BFO:SmO films were measured and shown as Fig. 11. It is obviously that the leakage current density of annealed BFO film is 2 orders of magnitude lower than that of the as-deposited BFO film. Therefore, the reduced oxygen vacancies contributed to the lower leakage current density in the annealed BFO films.

As we discussed earlier, the leakage current density of the BFO:SmO nanocomposite is much lower than that of the BFO films. Considering the nature that the leakage current in nanocomposites is controlled by the BFO phase and the relationship between the oxygen vacancies and the leakage current in BFO films, the much lower leakage current density in nanocomposite implies the reduced oxygen vacancies in the BFO phase. In the other side, it is worth noting that in Fig. 11 two curves for as-deposited and annealed BFO:SmO nanocomposites are almost overlapped, especially in the higher electric fields. This further

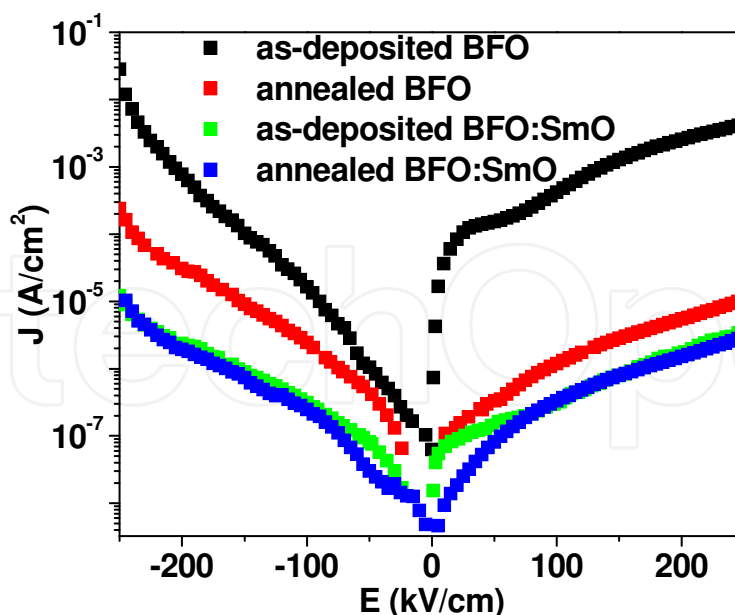


Fig. 11. Comparison of leakage current densities of as-deposited and annealed BFO and BFO:SmO films.

confirmed that the oxygen vacancies in the BFO phase were reduced and then the post-annealing shows little influence on them. Considering the microstructure of the BFO:SmO nanocomposites, one explanation for the reduced oxygen vacancies in BFO phase is that there is oxygen transportation from the SmO to the BFO. Theoretically, the possibility of oxygen transportation is proportional to the interface area. The vertical interfacial area of each BFO column is $2at$ in a nanocomposite system, where a is the average dimension of the column and t is the film thickness (MacManus-Driscoll et al., 2008). On the other hand, the lateral interfacial area for a pure BFO film on a Nb-STO substrate (assuming the same dimension) is simply $a \times a$. It is obvious that the interfacial area of BFO phase in the nanocomposite can be much higher (considering $a \sim 15$ nm and $t \sim 150$ nm). Then, the possibility of oxygen transportation from the SmO to the BFO in the nanocomposite is much larger than that from substrate to pure BFO film. In other words, the larger vertical interfacial area in BFO:SmO nanocomposites contribute to the reduction of leakage current density of the BFO phase, and so the reduced dielectric loss.

To further understand the dielectric and leakage properties, we investigated the leakage mechanism of nanocomposite BFO:SmO films. Figure 12 shows $\log(J)$ vs $\log(E)$ characteristics of as-deposited BFO, annealed BFO, and nanocomposite BFO:SmO films at positive bias. The slopes are close to 1 and the leakage currents show Ohmic behaviour at relatively lower electric fields. In the high electric field range ($> \sim 75$ kV/cm), the $\log(J)$ - $\log(E)$ plots are linear and the slopes are close to 2, which agree well with the SCLC mechanism. The SCLC is considered as a normal leakage behaviour and correlates with oxygen vacancies in BFO materials (Wang, et al., 2006). In addition, we also studied the J - E characteristics of as-deposited BFO, annealed BFO, and BFO:SmO films at negative bias. In the low electric field range (< 50 kV/cm), the $\log(J)$ vs $\log(E)$ plots are linear and the slopes are around 2 (not shown), indicating the conduction is controlled by SCLC. Figure 13 shows (a) $\ln(J/E^2)$ vs $(1/E)$ characteristic of as-deposited BFO film and (b) $\ln(J/E)$ vs $E^{1/2}$ characteristics of

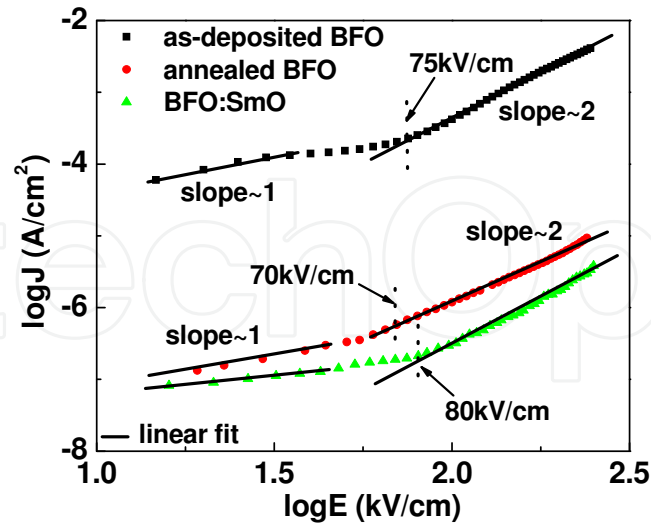


Fig. 12. $\log(J)$ vs $\log(E)$ characteristics of as-deposited BFO, annealed BFO, and BFO:SmO thin films at positive bias.

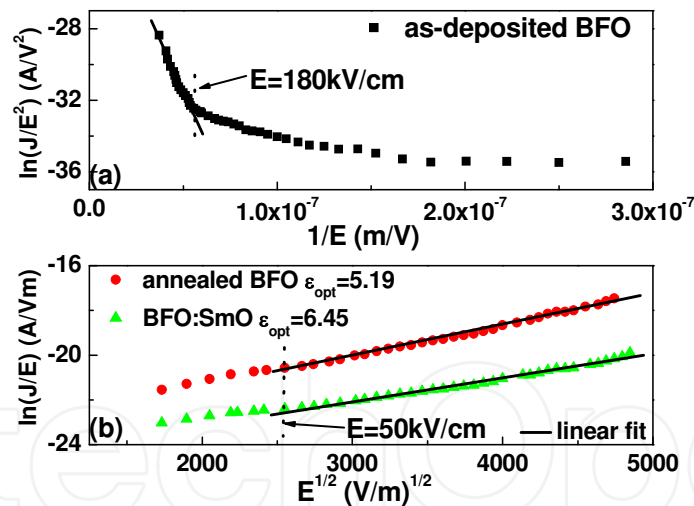


Fig. 13. (a) $\ln(J/E^2)$ vs $(1/E)$ characteristic of as-deposited BFO film; (b) $\ln(J/E)$ vs $E^{1/2}$ characteristics of BFO:SmO and annealed BFO films at negative bias. The calculated optical dielectric constants are shown.

BFO:SmO and annealed BFO films at negative bias. For the as-deposited BFO film, the leakage currents show F-N tunneling behaviour in the electric field above 180 kV/cm. On the other hand, the $\ln(J/E)-E^{1/2}$ plots of BFO:SmO and annealed BFO films show linear relation in the electric field above 50 kV/cm. The ϵ_{opt} of BFO:SmO and annealed BFO films, with values of 6.45 and 5.19 respectively, can be calculated from the slopes of $\ln(J/E)$ vs $E^{1/2}$ plots. The optical refractive index (n) can be determined from the optical dielectric constant

with a relationship of $n = \sqrt{\epsilon_{opt}}$. For BFO:SmO and annealed BFO films, the n can be evaluated as 2.54 and 2.28 respectively. The n can also be measured directly from the spectroscopic ellipsometry (SE) measurement through model based analysis. The measured n values are 2.42 and 2.58 at the wavelength of 633 nm for BFO:SmO and annealed BFO films, respectively. The n values calculated from slopes of $\ln(J/E)$ vs $E^{1/2}$ plots are in good agreement with the SE extracted results, strongly suggesting P-F emission behavior in the electric field range above 50 kV/cm. The P-F emission is commonly considered as acceptable leakage behaviour and the likely trap centre is Fe^{2+} in BFO films. Therefore, the leakage mechanisms of BFO:SmO nanocomposite films are the same as those of annealed BFO films. This is in consistent with the reduced V_{OS} in BFO phase in the nanocomposite films.

To summarize, self-assembled BFO:SmO nanocomposite films have been deposited with three-dimensional heteroepitaxy having an ordered nano-columnar structure on a large scale. The vertical strain is the dominant factor determining the out-of-plane lattice parameters and strain state of the BFO and SmO phases. The dielectric constant of the nanocomposite is not a function of strong vertical strain and can be modeled very well by an equivalent parallel circuit. The nanocomposite shows a lower than expected dielectric loss, due to the presence of a larger vertical interfacial area in the nanocomposite, causing a reduction of the oxygen depletion in the BFO phase relative to a pure BFO film. The present work represents a new way to enhance functionalities of oxide films by both strain coupling and increase of interfacial area in the vertical nanocomposite architecture.

5. Conclusions and future research

In conclusion, by detailed material design and fabrication, self-assembled nanocomposite oxide films with horizontal and vertical architectures have been achieved on YBCO:BZO and BFO:SmO systems respectively. The microstructures, physical properties, and relationships between them have been investigated. It has been found that the interfacial and strain engineering play a critical role to determine the nanostructure and then the unique functionalities. Future work will focus on the mechanism of self-assembly, the full conditions of material design, and the way to control the microstructures and functionalities. The self-assembled nanocomposite films with ordered nanostructure hold great promise for novel applications on microelectronics, optoelectronics, photonics, and energy storage (MacManus-Driscoll et al., 2008; Yang et al., 2009). The work in this chapter also opens up a new avenue to control a self-assembled system to create a desired nanostructure.

6. Acknowledgements

The authors acknowledge the support from the National Natural Science Foundation of China under Grant No. 11004145, the Natural Science of Jiangsu Province under Grant No. SBK201021263, and the "211 Project" grants of Soochow University. The work in Los Alamos National Laboratory was supported by the U. S. Department of Energy through the LANL/LDRD Program and the Center for Integrated Nanotechnologies.

7. References

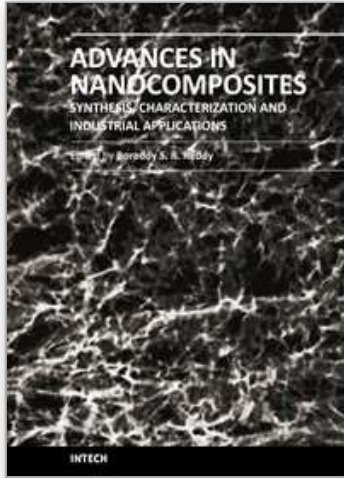
- Barnes, P. N.; Haugan, T. J.; Varanasi, C. V.; et al., (2004). Flux pinning behavior of incomplete multilayered lattice structures in $\text{YBa}_2\text{Cu}_3\text{O}_{7-d}$. *Appl. Phys. Lett.* 85, 4088-4090.
- Cai, C.; Holzapfel, B.; Hänisch, J.; et al., (2004). Direct evidence for tailorable flux-pinning force and its anisotropy in $\text{RBa}_2\text{Cu}_3\text{O}_{7-\delta}$ multilayers. *Phys. Rev. B*, 70, 212501
- Cheng, J. Y.; Ross, C. A.; Smith, H. I.; et al. (2006). Templated Self-Assembly of Block Copolymers: Top-Down Helps Bottom-Up. *Adv. Mater.* 18, 2505-2521.
- Choi, K. J.; et al., (2004). Enhancement of ferroelectricity in strained BaTiO_3 thin films. *Science*, 306, 1005-1009.
- Foltyn, S. R.; Civale, L.; MacManus-Driscoll, J. L.; et al., (2007). Materials science challenges for high-temperature superconducting wire. *Nat. Mater.*, 6, 631-642.
- Guiton, B. S. & Davies, P. K. (2007). Nano-chessboard superlattices formed by spontaneous phase separation in oxides. *Nat. Mater.* 6, 586-591.
- Haeni, J. H.; et al., (2004). Room-temperature ferroelectricity in strained SrTiO_3 . *Nature*, 430, 758-761.
- Haugan, T.; Barnes, P. N.; Wheeler, R.; et al., (2004). Addition of nanoparticle dispersions to enhance flux pinning of the $\text{YBa}_2\text{Cu}_3\text{O}_{7-x}$ superconductor. *Nature*. 430, 867-870.
- Huhtinen, H.; Schlesier, K.; & Paturi, P., (2009). Growth and *c*-axis flux pinning of nanostructured YBCO/BZO multilayers. *Supercond. Sci. Technol.* 22, 075019.
- Jia, C. L.; Nagarajan, V.; He, J. Q.; Houben, L.; et al., (2007). Unit-cell scale mapping of ferroelectricity and tetragonality in epitaxial ultrathin ferroelectric films. *Nat. Mater.* 6, 64-69.
- Jia, Q. X.; Foltyn, S. R.; Arendt, P. N.; et al., (2002). High-temperature superconducting thick films with enhanced supercurrent carrying capability. *Appl. Phys. Lett.* 80, 1601-1603.
- Joshi, P. C. & Cole, M. W.; (2000). Mg-doped $\text{Ba}_{0.6}\text{Sr}_{0.4}\text{TiO}_3$ thin films for tunable microwave applications. *Appl. Phys. Lett.* 77, 289-291.
- Junquera, J. & Ghosez, P.; (2003). Critical thickness for ferroelectricity in perovskite ultrathin films. *Nature*, 422, 506-509.
- Kang, S.; Goyal, A.; Li, J.; et al., (2006). High-Performance High- T_c Superconducting Wires. *Science*, 311, 1911-1914.
- Kang, S.; Goyal, A.; Li, J.; et al., (2007). Flux-pinning characteristics as a function of density of columnar defects comprised of self-assembled nanodots and nanorods in epitaxial $\text{YBa}_2\text{Cu}_3\text{O}_{7-d}$ films for coated conductor applications. *Physica C.*, 457, 41-46.
- Lee, H. N.; Christen, H. M.; Chisholm, M. F.; Rouleau, C. M.; et al., (2005). Strong polarization enhancement in asymmetric three-component ferroelectric superlattices. *Nature*, 433, 395-399.
- MacManus-Driscoll, J. L.; Foltyn, S. R.; Jia, Q. X.; et al., (2004). Strongly enhanced current densities in superconducting coated conductors of $\text{YBa}_2\text{Cu}_3\text{O}_{7-x} + \text{BaZrO}_3$. *Nat. Mater.* 3, 439-443.
- MacManus-Driscoll, J. L.; Zerrer, P.; Wang, H.; et al., (2008). Strain control and spontaneous phase ordering in vertical nanocomposite heteroepitaxial thin films. *Nat. Mater.* 7, 314-320.

- Maiorov, B.; Baily, S. A.; Zhou, H.; et al., (2009). Synergetic combination of different types of defect to optimize pinning landscape using BaZrO₃-doped YBa₂Cu₃O₇. *Nat. Mater.* 8, 398-404.
- Matthews, J.W. & Blakeslee, A. E.; (1974). Defects in epitaxial multilayers.1. Misfit dislocations. *J. Cryst. Growth* 27, 118-125.
- Michel, C.; Moreau, J. M.; Achenbach, G. D. ; Gerson, R.; et al., (1969). The atomic structure of BiFeO₃. 7, 701-704.
- Moshnyaga, V.; Damaschke, B.; Shapoval, O.; et al., (2003). Structural phase transition at the percolation threshold in epitaxial (La_{0.7}Ca_{0.3}MnO₃)_{1-x}:(MgO)_x nanocomposite films. *Nat. Mater.* 2, 247-252.
- Nagarajan, V.; et al., (2005). Misfit dislocations in nanoscale ferroelectric heterostructures. *Appl. Phys. Lett.* 86, 192910.
- Ohtomo, A.; Muller, D. A.; Grazul, J. L.; et al., (2002). Artificial charge-modulation in atomic-scale perovskite titanate superlattices. *Nature*, 419, 378-380.
- Ohtomo, A. & Hwang, H. Y.; (2004). A high-mobility electron gas at the LaAlO₃/SrTiO₃ heterointerface. *Nature*, 427, 423-426.
- Pan, A. V. ; Pysarenko, S. V., & Dou, S. X., (2006). Drastic improvement of surface structure and current-carrying ability in YBa₂Cu₃O₇ films by introducing multilayered structure. *Appl. Phys. Lett.* 88, 232506.
- Peurla, M.; Paturi, P.; Stepanov, Y. P.; et al., (2006). Optimization of the BaZrO₃ concentration in YBCO films prepared by pulsed laser deposition. *Supercond. Sci. Technol.* 19, 767-771.
- Ramesh, R. & Spaldin, N. A. (2007). Multiferroics: progress and prospects in thin films. *Nat. Mater.*, 6, 21-29.
- Reyren, N.; Thiel, S.; Caviglia, A. D.; et al., (2007). Superconducting Interfaces Between Insulating Oxides. *Science*, 317, 1196-1199.
- Sherman, V. O.; Tagantsev, A. K.; Setter, N.; Iddles, D.; et al., (2006). Ferroelectric-dielectric tunable composites. *J. Appl. Phys.* 99, 074104.
- Ueda, K. ; Tabata, H. & Kawai, T. (1998). Ferromagnetism in LaFeO₃-LaCrO₃ Superlattices. *Science*, 280, 1064-1066.
- Wang, C.; Takahashi, M.; Fujino, H; Zhao, X; et al., (2006). Leakage current of multiferroic (Bi_{0.6}Tb_{0.3}La_{0.1})FeO₃ thin films grown at various oxygen pressures by pulsed laser deposition and annealing effect. *J. Appl. Phys.* 99, 054104.
- Yamada, T.; Sherman, V. O.; Nöth, A.; Murali, P.; et al., (2006). Epitaxial/amorphous Ba_{0.3}Sr_{0.7}TiO₃ film composite structure for tunable applications. *Appl. Phys. Lett.* 89, 032905.
- Yang, H.; Wang, H.; Yoon, J.; et al., (2009). Vertical Interface Effect on the Physical Properties of Self-Assembled Nanocomposite Epitaxial Films. *Adv. Mater.*, 21, 3794-3798.
- Yang, H.; Wang, H.; Maiorov, B.; et al., (2009). Self-assembled multilayers and enhanced superconductivity in (YBa₂Cu₃O_{7-x})_{0.5}:(BaZrO₃)_{0.5} nanocomposite films. *J. Appl. Phys.*, 106, 093914.
- Zheng, H.; Wang, J.; Lofland, S. E.; et al. (2004). Multiferroic BaTiO₃-CoFe₂O₄ Nanostructures. *Science*, 303, 661-663.

Zheng, H.; Wang, J.; Mohaddes-Ardabili, L.; et al., (2004). Three-dimensional heteroepitaxy in self-assembled BaTiO₃-CoFe₂O₄ nanostructures. *Appl. Phys. Lett.* 85, 2035-2037.

IntechOpen

IntechOpen



Advances in Nanocomposites - Synthesis, Characterization and Industrial Applications

Edited by Dr. Boreddy Reddy

ISBN 978-953-307-165-7

Hard cover, 966 pages

Publisher InTech

Published online 19, April, 2011

Published in print edition April, 2011

Advances in Nanocomposites - Synthesis, Characterization and Industrial Applications was conceived as a comprehensive reference volume on various aspects of functional nanocomposites for engineering technologies. The term functional nanocomposites signifies a wide area of polymer/material science and engineering, involving the design, synthesis and study of nanocomposites of increasing structural sophistication and complexity useful for a wide range of chemical, physicochemical and biological/biomedical processes. "Emerging technologies" are also broadly understood to include new technological developments, beginning at the forefront of conventional industrial practices and extending into anticipated and speculative industries of the future. The scope of the present book on nanocomposites and applications extends far beyond emerging technologies. This book presents 40 chapters organized in four parts systematically providing a wealth of new ideas in design, synthesis and study of sophisticated nanocomposite structures.

How to reference

In order to correctly reference this scholarly work, feel free to copy and paste the following:

Hao Yang, Qingquan Meng, Run Zhao, Jun Yang and Weiwei Li (2011). Self-assembled Nanocomposite Oxide Films: Design, Fabrication, and Properties, *Advances in Nanocomposites - Synthesis, Characterization and Industrial Applications*, Dr. Boreddy Reddy (Ed.), ISBN: 978-953-307-165-7, InTech, Available from: <http://www.intechopen.com/books/advances-in-nanocomposites-synthesis-characterization-and-industrial-applications/self-assembled-nanocomposite-oxide-films-design-fabrication-and-properties>

INTECH
open science | open minds

InTech Europe

University Campus STeP Ri
Slavka Krautzeka 83/A
51000 Rijeka, Croatia
Phone: +385 (51) 770 447
Fax: +385 (51) 686 166
www.intechopen.com

InTech China

Unit 405, Office Block, Hotel Equatorial Shanghai
No.65, Yan An Road (West), Shanghai, 200040, China
中国上海市延安西路65号上海国际贵都大饭店办公楼405单元
Phone: +86-21-62489820
Fax: +86-21-62489821

© 2011 The Author(s). Licensee IntechOpen. This chapter is distributed under the terms of the [Creative Commons Attribution-NonCommercial-ShareAlike-3.0 License](#), which permits use, distribution and reproduction for non-commercial purposes, provided the original is properly cited and derivative works building on this content are distributed under the same license.

IntechOpen

IntechOpen